Journal of Materials Chemistry A

ROYAL SOCIETY OF CHEMISTRY

PAPER

View Article Online
View Journal | View Issue

Cite this: *J. Mater. Chem. A*, 2021, **9**, 22952

Balancing stability and Li-ion conductivity of $Li_{10}SiP_2O_{12}$ for solid-state electrolytes with the assistance of a body-centered cubic oxygen framework†

Bingkai Zhang,[a] Zhiwei He,[a] Jiajie Zhong,[a] Luyi Yang,[b] Zhan Lin *[a] and Feng Pan *[b]

Received 27th July 2021
Accepted 21st September 2021

DOI: 10.1039/d1ta06338c

rsc.li/materials-a

$Li_{10}MP_2S_{12}$ (LMPS, M = Ge, Sn, or Si) share an underlying body-centered cubic (bcc) anion framework enabling their high Li-ion conductivity. To take full use of the high conductivity of the bcc anion framework and boost the electrochemical stability, we have theoretically developed the chemistry of local structural motifs of LMPS to build the oxygen frameworks $Li_{10}SiP_2O_{12}$ (LSPO) and $Li_{19}Si_2P_4O_{23}Cl$ (LSPOCl), which combine good electrochemical stability and high Li conductivity. They exhibit a wider electrochemical stability window compared to their sulfur analogue. At the anode side, they form ionic conductive but electronic insulating phases that prevent further reduction. The bcc oxygen framework allows Li cooperative migration with a low migration barrier (~0.30 eV) in adjacent tetrahedral sites, which is most desirable for fast Li-ion conductors. The addition of halogen Cl contributes to the Li-ion migration because of the increased hybridization between the Si/P and Cl atoms. The LSPO and LSPOCl oxides with a bcc-type anion framework could be a viable way to overcome the trade-off between electrochemical stability and ionic conductivity.

1. Introduction

In electric vehicle batteries, safety concerns have been an obstacle for conventional rechargeable lithium batteries (LIBs) owing to their potential risks such as volatilization, flammability, and explosion.[1–3] Currently, solid-state lithium-ion electrolytes are being considered as potential replacements for liquid electrolytes due to the large electrochemical stability voltage window, high chemical stability, and diminished flammability.[4–6] Currently, the highest-conductivity inorganic solid-state electrolytes (ISEs) are in lithium thiophosphate systems, with $Li_7P_3S_{11}$ and materials isostructural to LMPS (with a space group $P4_2/nmc$), having room-temperature conductivities of up to 17 mS cm^{-1} and 25 mS cm^{-1}, respectively, even higher than those of organic liquid electrolyte counterparts (~10 mS cm^{-1}).[7–9] The reason behind the high Li-ion conductive ISEs is attributed to a body-centered cubic (bcc) sulfur anion framework that allows Li-ions to migrate within a network of energetically equivalent LiS_4 tetrahedral sites.[8,10,11] However, currently, there are three main obstacles for LMPS: (1) strong interfacial reactions at the cathode-electrolyte interface, (2) narrow electrochemical stability window, and (3) very poor moisture stability.[12]

In contrast, the oxygen-based analogues can avoid the above-mentioned interfacial stability (the interface between the high-voltage transition metal oxide cathode and ISEs) and moisture stability problems.[13–15] Recently, there have been few efforts toward the understanding of Li-ion diffusion of oxygen partially substituted $Li_{10}MP_2S_{12-x}O_x$, and it has been found that the presence of PO_4 units helps in structural stability without reducing Li-ion conductivity.[16,17] Tuning the two different local structural motifs ((M/P)S_4 and LiS_x units) by oxygenation within the rare bcc surface framework may well combine the stability with high Li conductivity. However, there are a few studies about the full substitution of sulfur by oxygen, that is, $Li_{10}MP_2O_{12}$ (LMPO), especially about structural properties, electrochemical stability, and Li-ion diffusion in LMPO. Whether this lack of good LMPO conductors is intrinsic or a result of the fact that they may be more difficult to synthesize is not yet clear. To date, just one experimental study demonstrated the feasibility of the synthesis of $Li_{10}SiP_2O_{12}$.[18]

Here, using density functional theory (DFT) and molecular dynamics simulations coupled with the Pymatgen code, we have investigated the crystal structures of $Li_{10}SiP_2O_{12}$ (LSPO) and its chlorine (Cl)-doped one $Li_{19}Si_2P_4O_{23}Cl_1$ (LSPOCl), and focused

[a]Guangzhou Key Laboratory of Clean Transportation Energy Chemistry, School of Chemical Engineering and Light Industry, Guangdong University of Technology, Guangzhou 510006, China. E-mail: zhanlin@gdut.edu.cn

[b]School of Advanced Materials, Peking University, Shenzhen, China. E-mail: panfeng@pkusz.edu.cn

† Electronic supplementary information (ESI) available. See DOI: 10.1039/d1ta06338c

on three issues: (i) the structural and electrochemical stability, (ii) the Li-ion diffusivity and the Li-ion transport mechanism, and (iii) the O–Cl mixed effects on the stability and ionic conductivity.

2. Results and discussion

2.1. Structural properties, phase stability, and electrochemical stability

We employ the well-studied $Li_{10}SiP_2S_{12}$ (LSPS) framework to provide an insight into the influence of full oxygenation that is $Li_{10}SiP_2O_{12}$. As shown in Fig. 1a, the LSPO structure has the following properties: (i) Octahedrally coordinated lithium (4d sites) is edge-shared with 4d $(P/Si)O_4$ tetrahedra along the *c*-axis and corner-shared with 2b PO_4 tetrahedra along the *a*- and *b*-axes, forming the backbone of the structure. (ii) The two tetrahedrally coordinated sites (the 8f and 16h sites) form one-dimensional chains of edge-sharing tetrahedra. Upon substituting S with O in LSPS, the increased hybridization (covalency) between the Si/P and O elements can shorten the bond length between the cation and anion, and thus reduces the lattice parameters. As expected, after the optimization, the lattice parameters of LSPO (Fig. 1a) are $a = b = 7.08$ Å, and $c = 10.41$ Å ($\alpha = 87.56°$, $\beta = 91.12°$, and $\gamma = 90.06°$). The lattice parameters calculated for LSPO are much smaller than those of LSPS ($a = b = 8.75$ Å, and $c = 12.89$ Å ($\alpha = 88.56°$, $\beta = 91.07°$, and $\gamma = 89.33°$)). Therefore, the volume of the Li-ion diffusion channel in LSPO is also smaller than that in LSPS. As suggested by previous studies, the contractible diffusion channel within a given crystal structure may increase the Li-ion migration activation energy and weaken ionic conductivity.[19–21] But the Coulomb interactions among Li-ions may increase Li-ion mobility because of the shortened Li–Li distances in the *c*-axis and *ab*-plane, making the overall effect on the migration barrier unclear. In addition, using the GCLP and DFT-computed bulk energy of LSPO, the compositions that appeared in the Li_2O–P_2O_5–SiO_2 phase space are shown in Fig. 1b. There is only one combination for LSPO decomposition or synthesis that is the decomposition of LSPO into ternary Li_3PO_4 and Li_4SiO_4, with a decomposition energy of 91.23 meV per atom. Based on the definition of phase decomposition energy ($E_{pd} = E(\text{LSPO}) - E(Li_3PO_4) - E(Li_4SiO_4)$), a positive value means the decomposition is thermodynamically unfavorable. Thus, LSPO shows very good phase stability.

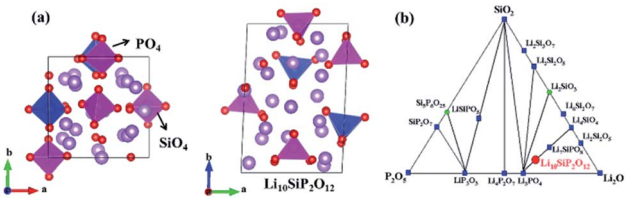

Fig. 1 (a) Top (left inset) and side (right inset) views of the LSPO crystal structure. (b) Compositions that appeared in the Li_2O–P_2O_5–SiO_2 phase space along with LSPO. The purple, red, and yellow spheres represent Li, O, and S atoms, respectively.

Except for the smaller lattice parameters, the electronic structures (Fig. 2a) as reflected by the total density of states (TDOS) for LSPS, LSPO, and LSPOCl show that the oxygenation greatly enlarges the bandgap ($\Delta_g = 5.54$ eV (5.21 eV) *vs.* 2.44 eV for the LSPO (LSPOCl) *vs.* the LSPS, respectively) because the strong hybridization of Si/P with O in $(Si/P)O_4$ units lowers the oxygen electron states. LSPO and LSPOCl are wide-bandgap insulators with limited electrical conductivity. While the large bandgaps of LSPO and LSPOCl suggest high electrochemical stability, the actual stability also depends on the alignment of the bands relative to the Li metal anode Fermi level and the cathode conduction band. The energy band of the Fermi level or conduction band can be directly converted to lithium chemical potential using the above equation ($\mu_{Li} = \mu_{Li}^0 - eV$) detailed in the computational section. After examining the phase diagram of μ_{Li} ranging from Li metal potential (0 V) to the cathodic voltage regime (5 V), we have determined the "stability window" *versus* bulk Li for LSPO, LSPOCl, and the reference ISEs such as LSPS, as shown in Fig. 2b, c and d, respectively. The Li uptake processes of per formula unit (f.u.) of LSPO and LSPOCl against voltage *vs.* Li/Li^+ are shown in Fig. S1 of the ESI.† For LSPO (Fig. 2b), at the Li-metal anode (from 0 to 0.22 V) LSPO decomposes into $Li_{21}Si_5$, $Li_{13}Si_4$, Li_7Si_3, Li_2O, and Li_3P. The formation of electrically conductive Li-metal alloy makes the interphase an MCI (mixed ionic–electronic conducting interphase) leading to the continued decomposition of LSPO. From 0.22 to 0.68 V, LSPO begins to decompose into Li_2O, Li_4SiO_4, and Li_3P which likely functions as an SEI (solid electrolyte interphase) due to the poor electronic conductivity. At the anode side 0.68 V to the cathode side 3.46 V, LSPO theoretically decomposes into Li_4SiO_4 and Li_3PO_4 whose bandgaps are large enough ($\Delta_g = 5.09$ and 5.84 eV) to block electrons but allow Li-ion transport. At the cathode side 3.46 V, LSPO will decompose into LiO_8 ($\Delta_g = 0$ eV), Li_3PO_4, Li_2SiO_3, and Li ($\Delta_g = 0$ eV) as it makes the interphase an MCI. Thus, although the absolute

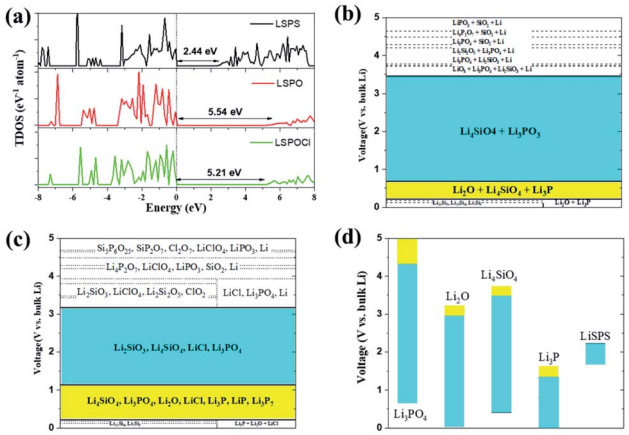

Fig. 2 (a) Total density of states of LSPS, LSPO, and LSPOCl, respectively. (b and c) The voltage profile and phase equilibria of LSPO and LSPOCl solid electrolytes upon lithiation and delithiation that determine the anodic and cathodic reactions, respectively. (d) Electrochemical stability windows (cyan bar). The yellow region reflects the possible extension of the electrochemical stability window.

electrochemical stability window of LSPO does not exist, decomposition products are electronically insulating and Li-conducting at 0.22 to 3.46 V and can inhibit further decomposition, so the electrochemical stability window is suggested in the range of 0.68 to 3.46 V (in the cyan region of Fig. 2b) and the extended range of 0.22 to 0.68 V (in the yellow region of Fig. 2b) where the interphases are SEI-like compounds.

In that spirit, we suggest that LSPOCl can be electrochemically stable in the window of 1.14 to 3.17 V (in the cyan region of Fig. 2c) where the decomposition phases Li_2SiO_3, Li_4SiO_4, LiCl, and Li_3PO_4 are also good ionic conductors and electronic insulators. The SEI-like interphases in the range of 0.22 to 1.14 V (in the yellow region of Fig. 2c) may further widen its electrochemical window. The addition of Cl may contribute to the formation of a passivating SEI containing LiCl that prevents further reduction. In addition, for the phase equilibria of LSPO at 0 V or against Li metal such as Li_3PO_4, Li_4SiO_4, Li_2O, and Li_3P, the electrochemical stability calculations (Fig. 2d) show that they exhibit a wider stability window, especially for Li_3PO_4 and Li_4SiO_4, which further protects LSPO and LSPOCl from decomposition. Indeed, many experimental results prove that the formation of passivating SEI leads to a wider electrochemical stability window in principle than in reality.[22–25] Lastly, such DFT estimated stability windows indicate the better inherent stability and performance of LSPO and LSPOCl than that of LSPS.

2.2. Li-ion migration mechanism in LSPO and LSPOCl

The Li diffusion properties of ISEs will change with anion substitution, so it is important to evaluate the Li-ion mobility (Li-ion migration activation energy) and transport mechanism in the bcc oxygen sublattice. Previous studies suggest that the substitution of sulfur by oxygen in the thio-LISICON leads to an increase of Li-ion migration activation energy, such as Li_3PS_4 and Li_3PO_4 as well as $Li_4P_2S_7$ and $Li_4P_2O_7$.[21] The reason for the high migration barrier may come from the smaller volume and reduced polarizability of oxides, which increases the electrostatic interactions between the Li-ion and the host structure. On the other hand, the bcc oxygen framework also reduces the *c*-axis lattice constant and thus reduces the Li–Li distance (up to 0.6 Å decrease). This effect may increase the Coulomb interactions among Li-ions, and thus decreases the activation energy of cooperative migration. Therefore, it is necessary to study the Li-ion migration barrier and the transport mechanism. Fig. 3a shows the possible diffusion network consisting of *c*-axis diffusion (Li_1–Li_2–Li_1) and interchannel diffusion in the *ab*-plane (Li_1–Li_3–Li_1). The distinct Li sites are labeled as 1, 2, and 3. By applying the AIMD simulation, Fig. 3b shows the Li-ion diffusion trajectory represented as dots including Li_1/Li_2 (purple dots) and Li_3 (pink dots). The diffusion in the *ab*-plane becomes apparent over 750 K (Li_3-ions (pink dots) are involved in the whole diffusion). The AIMD results suggest that Li-ion diffusion in the *c*-axis direction is much more favorable than that in the *ab*-plane, and the Li-ion diffusion pattern changes from one-dimensional (1D) to three-dimensional (3D) with increasing temperature.

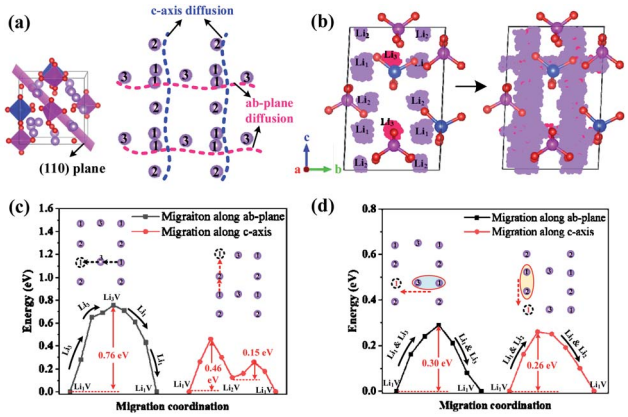

Fig. 3 (a) Schematic diagram of the (110) plane of LSPO. (b) Li-ion trajectory dots in LSPO obtained from *ab initio* molecular dynamics (AIMD) simulations at 300 K (left) and 800 K (right). The purple dots represent the original Li_1 and Li_2 ions and the pink dots represent original Li_3 ions. (c and d) Energy diagrams of Li-ion migration in LSPO (c) *via* the one Li-ion direct-hopping mechanism, (d) *via* two Li-ion cooperative migration mechanisms along the *ab*-plane and c-axis. The vacancy of Li_x is labeled as Li_xV. The purple, red, blue, and pink spheres represent Li, O, Si, and P atoms, respectively.

To investigate the Li-ion transport mechanism in more detail, the climbing image-nudged elastic band (Cl-NEB) calculations are carried out as shown in Fig. 3c and d. Two migration models with the assistance of Li-ion vacancies are considered: (i) one Li-ion direct-hopping migration (Fig. 3c) and (ii) two Li-ion cooperative migration (Fig. 3d). The cooperative migration model is that two adjacent Li ions migrate in pairs and displace the Li-ions into their neighboring sites.[26–28] The detailed results for the energy path of Li-ion cooperative migration in structures along the *ab*-plane and *c*-axis are shown in Fig. S2 and S3 of the ESI,† respectively. Such a mechanism has long been believed to dominate cation migration in LMPS,[29] $Li_{1.3}Al_{0.3}Ti_{1.7}(PO_4)_3$ (LATP),[30] and $Li_7La_3Zr_2O_{12}$ (LLZO),[31] but has not been elucidated in LSPO. For one Li direct-hoping migration (Fig. 3c), the calculated energy profile along the *ab*-plane with the Li_1 and Li_3 sites has a barrier of 0.76 eV and that along the *c*-axis with the Li_1 and Li_2 sites has a barrier of 0.46 eV. For the two Li-ion cooperative migration (Fig. 3d), Li_1 & Li_2 and Li_1 & Li_3 cooperate to transport along the *ab*-plane and *c*-axis, respectively. Not surprisingly, the energy profile shows that cooperative migration has much lower activation energy (0.30 eV and 0.26 eV along the *ab*-plane and *c*-axis, respectively) than one Li-ion direct migration. The calculated activation energy of 0.26–0.30 eV for LSPO is comparable to the value of ~0.30 eV calculated for the LLZO composition.[32,33] Therefore, in bcc-type lattices formed by oxygen, the Li migration barrier arising from cooperative migration is close to that of other ISEs, suggesting an affordable Li superionic conductor.

Based on the above discussion, LSPO has a wider electrochemical stability window (Fig. 2b), but the use of oxygen comes at the cost of a migration barrier at least 0.90 eV higher than that of sulfide LSPS. Substituting partial oxygen with halogen Cl, that is LSPOCl, also maintains a wider electrochemical

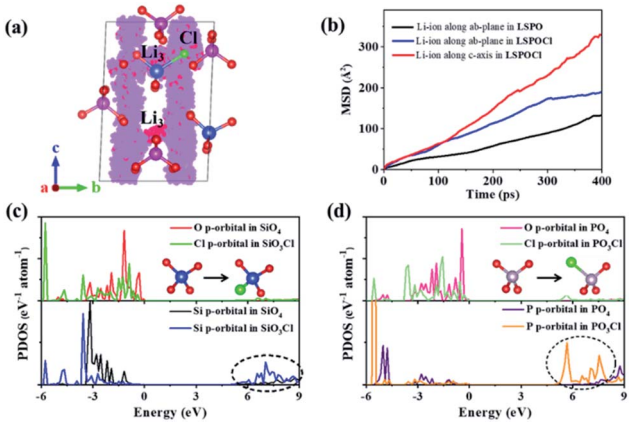

Fig. 4 (a) Li-ion trajectory dots in LSPOCl obtained from AIMD simulations at 800 K. The purple dots represent the original Li_1 and Li_2 ions and the pink dots represent original Li_3 ions. (b) Mean square displacements (MSDs) of Li-ions along the *c*-axis and *a*-axis crystallographic directions are obtained from the AIMD trajectory at 800 K within LSPO and LSPOCl. (c and d) Partial density of states (PDOS) for the p-orbitals of O, Cl, P, and Si before and after Cl-doping in (c) SiO_4 and SiO_3Cl and (d) PO_4 and PO_3Cl, respectively. Insets show the (Si/P)O_4 and (Si/P)O_3Cl structural units. The green, red, blue, and pink spheres represent Cl, O, Si, and P atoms, respectively.

stability window (Fig. 2c), but the effect on the ion mobility is unclear. To study the effect of Cl-doping on Li-ion mobility, we have done the AIMD simulation in LSPOCl, as shown in Fig. 4a. The Li-ion trajectory dots overlap significantly at the upper Li_3 site with the Cl-dopant, but less overlapping occurs at the lower Li_3 site. This suggests that Cl-doping facilitates the diffusion of Li_3 ions from one *c*-axis channel to the adjacent one. The mean square displacement (MSD) of Li ions along the *c*- and *a*-axis directions determined from the AIMD trajectory of 400 ps reveals a nearly isotropic 3D Li-diffusion pattern (Fig. 4b). Such 3D diffusion behaviour (blue line in Fig. 4b) within the O–Cl mixed framework is in slight contrast to the anisotropic 3D diffusion in pure LSPO (black line in Fig. 4b), also suggesting that the Cl-doping increases the Li-ion diffusion along the *ab*-plane. The results are consistent with previous studies that have found that Li-ion conductivity in Cl-doped LSPS is improved compared to pure LSPS.[29]

To further explain the effects of the Cl-dopant on conductivity, Fig. 4c and d show the partial density of states (PDOS) of LSPO and LSPOCl for the O-, Si-, P-, and Cl- p-orbitals, respectively. The hybridization between Si/P and O atoms leads to redox stability and also the positive charges of Si/P atoms. But compared with the (Si/P)O_4 units, (Si/P)O_3Cl units show the following two differences. The first one is that the orbitals of Si or P shift downward and lower the electron states due to the charge transfer from Cl atoms to Si atoms in the SiO_3Cl anions. The second one is that the shallow levels located near the bottom of the lowest unoccupied molecular orbital (LUMO) at approximately 3.0 eV in the SiO_4 anions turn into deep levels (appeared clear peak value increases) in the (Si/P)O_3Cl units. These levels are related to charge/electron trapping processes in materials. In the (Si/P)O_3Cl units, the deep levels near the LUMO are expected to weaken the positive charge of the Si/P ions, which reduces the electrostatic interaction between Li ions and the host structure, leading to a lower Li-ion migration barrier. In other words, the increasing hybridization between the Si/P and Cl atoms pulls the electron density away from the Li-ion diffusion channel along the *c*-axis direction. This effect helps to liberate adjacent Li-ions and leads to a levelling off of energy potential of Li-ions that permits high ionic conductivity, which has been proven by experimental studies.[34] Therefore, we suggest that hybridizing the anion states is a viable way to increase ionic conductivity.

3. Conclusions

In summary, we have explored the chemistry of local structural motifs within the LMPS framework to overcome the trade-off between electrochemical stability and ionic conductivity. LSPO and LSPOCl exhibit a wider electrochemical stability window compared to their sulfur analogue LSPS. When in contact with Li metal, thermodynamic DFT analysis predicts LSPO and LSPOCl to be fully reduced to products including Li_2O, Li_4SiO_4, LiCl, *etc.* These decomposition products prevent further reduction of LSPO and LSPOCl as they are electronic insulators and ionic conductors. Furthermore, the lattice formed by O^{2-} anions offers strong Li–Li interactions, and the Li migration barrier in bcc-type anion frameworks is also lower than that of other close-packed types (for example, γ-Li_3PO_4). Cooperative migration both in the *ab*-plane and *c*-axis lowers the migration barriers. Cl-doping leads to the variation in the electronic structures and enables further enhancement of the mobility of Li-ions. The Cl-doping effect also suggests that hybridizing the anion states is a viable way to overcome the trade-off between oxidation stability and ionic conductivity. Therefore, compared with traditional individual Li-ion diffusion behavior, Li-ion cooperative migration takes advantage of creating a novel 3D Li-ion diffusion path with lower energy barriers for LISICON-like LSPO solid-state electrolyte to enable fast Li-ion diffusion for advanced all-solid Li-ion batteries.

4. Methods

All DFT calculations are carried out using the Vienna *ab initio* simulation package (VASP)[35] within the projector augmented wave (PAW) approach.[36] The generalized gradient approximation (GGA) is adopted in the parameterization of Perdew, Burke, and Ernzerhof (PBE) to describe the exchange-correlation functional.[37,38] A supercell containing 4 formula units (f.u.) of $Li_{10}SiP_2O_{12}$ as a model is used for structural optimization and Li-ion migration calculations. A *k*-mesh ($2 \times 2 \times 2$) is generated using the Monkhorst–Pack method to sample the Brillouin zone. The evaluation of the migration barrier of Li-ions is carried out using the supercell with 4 f.u. by the Cl-NEB method[39] as implemented in the VASP. The Li-ion diffusivity in LSPO and LSPOCl is studied using AIMD simulations with the GGA-PBE functional as implemented in VASP software. The gamma-only *k*-point and a supercell containing 4 f.u. of Li_{10}-SiP_2O_{12} are considered. The time step and the total period cover

for AIMD are 1 fs and 400 ps, respectively. MSD is the average of the total number of Li-ions over the total period. The NVE ensemble at elevated temperature, 800 K, is used during AIMD.

To study the electrochemical stability of the oxides with respect to a range of possible electrochemical redox products, we have evaluated the stability of LSPO and LSPOCl in the range of applied voltage, V. Here, to check the effect of the Cl-dopant on ionic conductivity, one Cl atom is doped with the oxygen of PO_4 or SiO_4 units in four 4 f.u. LSPO, that is $(P/Si)O_4 \rightarrow (P/Si)O_3Cl$. To maintain the charge compensation, one Li atom along the *c*-axis is deleted from the bulk structure since Li atoms in the *c*-axis channel are energetically equivalent in LSPO. The applied voltage can be directly converted to Li chemical potential (μ_{Li}) using equation ($\mu_{Li} = \mu_{Li}^0 - eV$) neglecting overpotential effects, where μ_{Li}^0 is the lithium chemical potential in Li metal and *e* is the elementary charge. The electrochemical stability window of the material corresponds to the range of voltage over which it is stable (exactly on the grand potential convex hull). The grand potential convex hull at a given V is formed by the grand potentials of a set of phases and their linear combinations that minimize the grand potential of LSPO and LSPOCl. Phase diagrams are constructed using the grand canonical linear programming (GCLP) method and the database consisting of DFT-computed bulk energies of crystals, as available in the Open Quantum Materials Database (OQMD).[40–43] The above approaches are implemented within Pymatgen (Python materials genomics), which is a robust, open-source Python library for materials analysis. Details of the methodology employed are shown in the usage website: https://www.pymatgen.org/usage.html.

Conflicts of interest

There are no conflicts to declare.

Acknowledgements

This work was supported by the GuangDong Basic and Applied Basic Research Foundation (2020A1515110046).

Notes and references

1 Y. Tian, *et al.*, *Chem. Rev.*, 2021, **121**, 1623–1669.
2 A. M. Abakumov, S. S. Fedotov, E. V. Antipov and J.-M. Tarascon, *Nat. Commun.*, 2020, **11**, 4976.
3 Y. Ji, Z.-W. Yin, Z. Yang, Y.-P. Deng, H. Chen, C. Lin, L. Yang, K. Yang, M. Zhang, Q. Xiao, J.-T. Li, Z. Chen, S.-G. Sun and F. Pan, *Chem. Soc. Rev.*, 2021, **50**, 10743–10763.
4 Y. Gao, A. M. Nolan, P. Du, Y. Wu, C. Yang, Q. Chen, Y. Mo and S.-H. Bo, *Chem. Rev.*, 2020, 9b00747.
5 B. Zhang, R. Tan, L. Yang, J. Zheng, K. Zhang, S. Mo, Z. Lin and F. Pan, *Energy Storage Maters*, 2018, **10**, 139–159.
6 H. Xu, Y. Yu, Z. Wang and G. Shao, *Energy Environ. Mater.*, 2019, **2**, 234–250.
7 N. Kamaya, *et al.*, *Nat. Mater.*, 2011, **10**, 682–686.
8 Y. Wang, W. D. Richards, S. P. Ong, L. J. Miara, J. C. Kim, Y. Mo and G. Ceder, *Nat. Mater.*, 2015, **14**, 1026–1031.
9 S. P. Ong, Y. Mo, W. D. Richards, L. Miara, H. S. Lee and G. Ceder, *Energy Environ. Sci.*, 2013, **6**, 148–156.
10 F. Wu, W. Fitzhugh, L. Ye, J. Ning and X. Li, *Nat. Commun.*, 2018, **9**, 4037.
11 Y. Mo, S. P. Ong and G. Ceder, *Chem. Mater.*, 2012, **24**, 15–17.
12 P. Lu, L. Liu, S. Wang, J. Xu, J. Peng, W. Yan, Q. Wang, H. Li, L. Chen and F. Wu, *Adv. Mater.*, 2021, 2100921.
13 G. Liu, D. Xie, X. Wang, X. Yao, S. Chen, R. Xiao, H. Li and X. Xu, *Energy Storage Maters*, 2019, **17**, 266–274.
14 Y. Deng, C. Eames, J.-N. Chotard, F. Lalère, V. Seznec, S. Emge, O. Pecher, C. P. Grey, C. Masquelier and M. S. Islam, *J. Am. Chem. Soc.*, 2015, **137**, 9136–9145.
15 X. Zhao, Z. Zhang, X. Zhang, B. Tang, Z. Xie and Z. Zhou, *J. Mater. Chem. A*, 2018, **6**, 2625–2631.
16 K.-H. Kim and S. W. Martin, *Chem. Mater.*, 2019, **31**, 3984–3991.
17 S. Banerjee, X. Zhang and L.-W. Wang, *Chem. Mater.*, 2019, **31**, 7265–7276.
18 S. Song, Z. Dong, F. Deng and N. Hu, *Funct. Mater. Lett.*, 2018, **11**, 1850039.
19 Y. A. Du and N. Holzwarth, *J. Electrochem. Soc.*, 2007, **154**, A999.
20 N. D. Lepley, N. A. W. Holzwarth and Y. A. Du, *Phys. Rev. B: Condens. Matter Mater. Phys.*, 2013, **88**, 2991–3000.
21 N. D. Lepley and N. A. W. Holzwarth, *J. Electrochem. Soc.*, 2012, **159**, A538–A547.
22 K. Takada, N. Ohta, L. Zhang, X. Xu, B. T. Hang, T. Ohnishi, M. Osada and T. Sasaki, *Solid State Ionics*, 2012, **225**, 594–597.
23 C. Wang, *et al.*, *Nano Energy*, 2018, **53**, 168–174.
24 B. R. Shin, Y. J. Nam, D. Y. Oh, D. H. Kim, J. W. Kim and Y. S. Jung, *Electrochim. Acta*, 2014, **146**, 395–402.
25 S. Wenzel, S. Randau, T. Leichtweiß, D. A. Weber, J. Sann, W. G. Zeier and J. Janek, *Chem. Mater.*, 2016, **28**, 2400–2407.
26 X. He, Y. Zhu and Y. Mo, *Nat. Commun.*, 2017, **8**, 15893.
27 S. Shi, P. Lu, Z. Liu, Y. Qi, L. G. Hector, H. Li and S. J. Harris, *J. Am. Chem. Soc.*, 2012, **134**, 15476–15487.
28 Z. Zhang, Z. Zou, K. Kaup, R. Xiao, S. Shi, M. Avdeev, Y. S. Hu, D. Wang, B. He and H. Li, *Adv. Energy Mater.*, 2019, **9**, 1902373.
29 B. Zhang, L. Yang, L.-W. Wang and F. Pan, *Nano Energy*, 2019, **62**, 844–852.
30 B. Zhang, Z. Lin, H. Dong, L.-W. Wang and F. Pan, *J. Mater. Chem. A*, 2020, **8**, 342–348.
31 Y. Chen, E. Rangasamy, C. Liang and K. An, *Chem. Mater.*, 2015, **27**, 5491–5494.
32 R. Jalem, M. J. D. Rushton, W. Manalastas, M. Nakayama, T. Kasuga, J. A. Kilner and R. W. Grimes, *Chem. Mater.*, 2015, **27**, 2821–2831.
33 S. Adams and R. P. Rao, *J. Mater. Chem.*, 2012, **22**, 1426–1434.
34 S. Li, Z. Huang, Y. Xiao and C. Sun, *Mater. Chem. Front.*, 2021, **5**, 5336–5343.
35 G. Kresse and J. Furthmüller, *Comput. Mater. Sci.*, 1996, **6**, 15–50.
36 P. E. Blöchl, *Phys. Rev. B: Condens. Matter Mater. Phys.*, 1994, **50**, 17953–17979.

37 G. Kresse and J. Furthmüller, *Phys. Rev. B: Condens. Matter Mater. Phys.*, 1996, **54**, 11169–11186.
38 J. P. Perdew, J. A. Chevary, S. H. Vosko, K. A. Jackson, M. R. Pederson, D. J. Singh and C. Fiolhais, *Phys. Rev. B: Condens. Matter Mater. Phys.*, 1992, **46**, 6671–6687.
39 G. Henkelman, B. P. Uberuaga and H. Jónsson, *J. Chem. Phys.*, 2000, **113**, 9901–9904.
40 Z. Deng, Z. Zhu, I.-H. Chu and S. P. Ong, *Chem. Mater.*, 2017, **29**, 281–288.
41 F. Han, Y. Zhu, X. He, Y. Mo and C. Wang, *Adv. Energy Mater.*, 2016, **6**, 1501590.
42 Y. Zhu, X. He and Y. Mo, *J. Mater. Chem. A*, 2015, **4**, 3253–3266.
43 Y. Zhu, X. He and Y. Mo, *ACS Appl. Mater. Interfaces*, 2015, **7**, 23685–23693.